ACS NANO
Cite This: ACS Nano 2019, 13, 449–457
www.acsnano.org

ARTICLE

Soft Three-Dimensional Microscale Vibratory Platforms for Characterization of Nano-Thin Polymer Films

Kewang Nan,[†,◆] Heling Wang,[‡,◆] Xin Ning,[§,◆] Kali A. Miller,[∥] Chen Wei,[‡] Yunpeng Liu,[†] Haibo Li,[‡,⊥] Yeguang Xue,[‡] Zhaoqian Xie,[‡] Haiwen Luan,[‡] Yihui Zhang,[#] Yonggang Huang,*[,‡] John A. Rogers,*[,▽] and Paul V. Braun*[,○]

[†]Department of Mechanical Science and Engineering, University of Illinois at Urbana−Champaign, Urbana, Illinois 61801, United States

[‡]Department of Civil and Environmental Engineering, Mechanical Engineering, Materials Science and Engineering, and Center for Bio-Integrated Electronics, Northwestern University, Evanston, Illinois 60208, United States

[§]Department of Aerospace Engineering, Pennsylvania State University, State College, Pennsylvania 16802, United States

[∥]Department of Chemistry, University of Illinois at Urbana−Champaign, Urbana, Illinois 61801, United States

[⊥]School of Naval Architecture, Ocean and Civil Engineering (State Key Laboratory of Ocean Engineering), Shanghai Jiaotong University, Shanghai 200000, China

[#]Center for Flexible Electronics Technology and Center for Mechanics and Materials; AML, Department of Engineering Mechanics, Tsinghua University, Beijing 100084, China

[▽]Center for Bio-Integrated Electronics, Department of Materials Science and Engineering, Biomedical Engineering, Chemistry, Mechanical Engineering, Electrical Engineering, and Computer Science, and Neurological Surgery, Simpson Querrey Institute for Nano/biotechnology, McCormick School of Engineering, and Feinberg School of Medicine, Northwestern University, Evanston, Illinois 60208, United States

[○]Department of Materials Science and Engineering, Frederick Seitz Materials Research Laboratory, and Beckman Institute for Advanced Science and Technology, University of Illinois at Urbana−Champaign, Urbana, Illinois 61801, United States

Supporting Information

ABSTRACT: **Vibrational resonances of microelectromechanical systems (MEMS) can serve as means for assessing physical properties of ultrathin coatings in sensors and analytical platforms. Most such technologies exist in largely two-dimensional configurations with a limited total number of accessible vibration modes and modal displacements, thereby placing constraints on design options and operational capabilities. This study presents a set of concepts in three-dimensional (3D) microscale platforms with vibrational resonances excited by Lorentz-force actuation for purposes of measuring properties of thin-film coatings. Nanoscale films including photodefinable epoxy, cresol novolak resin, and polymer brush with thicknesses as small as 270 nm serve as the test vehicles for demonstrating the advantages of these 3D MEMS for detection of multiple physical properties, such as modulus and density, within a single polymer sample. The stability and reusability of the structure are demonstrated through multiple measurements of polymer samples using a single platform, and *via* integration with thermal actuators, the temperature-dependent physical properties of polymer films are assessed. Numerical modeling also suggests the potential for characterization of anisotropic mechanical properties in single or multilayer films. The findings establish unusual opportunities for interrogation of the physical properties of polymers through advanced MEMS design.**

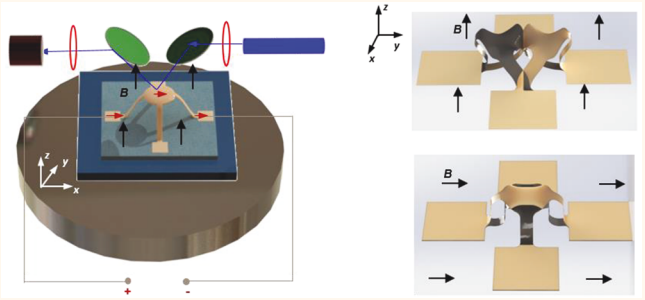

KEYWORDS: *three-dimensional structures, microelectromechanical systems, multimodal resonance, polymer mechanics, anisotropic properties, lorentz-force actuation*

Microelectromechanical systems (MEMS) with tailored mechanical vibratory resonances address a range of applications in mass detection,[1−3] microscale rheology,[4−6] energy harvesting,[7−11] wearable sensors,[12,13]

Received: September 3, 2018
Accepted: November 20, 2018
Published: November 20, 2018

DOI: 10.1021/acsnano.8b06736
ACS Nano 2019, 13, 449−457

and soft robotics.[14,15] Existing MEMS are largely based on two-dimensional (2D) geometries such as cantilevered beams,[16] doubly clamped bridges/wires,[17] and suspended plates,[18] which present limited numbers of accessible vibration modes and configurations of modal displacements. Consequently, the operation of most MEMS relies on a single vibration mode, thereby restricting their capability, for example, in detecting anisotropic mechanical properties in certain biological[19−21] and composite[22−26] thin-film materials. Access to multimodal resonances in 2D MEMS platforms typically requires non-idealities and asymmetries in nanomechanical resonators,[27] or advanced actuation techniques using collections of piezoelectric components[28] or patterned illumination with structured laser beams,[29] but the consequent engineering complications create challenges in scaling and adapting to complex materials systems. A potential alternative strategy relies on three-dimensional (3D) vibrational structures with multimodal and tunable resonances,[30,31] formed by microfabrication and controlled assembly.[32−39] Reported methods in actuation *via* thin-film piezoelectric elements require, however, multistep fabrication processes, and they operate over a limited range of frequencies.

In this study, we introduce a set of experimental and theoretical approaches to the design and fabrication of 3D microscale frameworks as vibratory platforms with integrated circuit elements for Lorentz-force actuation and localized heating. The assembly process exploits techniques in deterministic mechanical buckling[36−39] on elastomeric substrates. The key features of these systems are their (1) high resonant frequencies, accessible *via* a combination of Lorentz-force actuation and small characteristic dimensions, (2) diverse, multimodal motions controlled through orientation of the actuation force and design of the 3D layouts, and (3) low overall tensile stiffnesses enabled by the use of thin polymers for the structural elements. The results represent promising tools for measurement of both mass and modulus in isotropic and anisotropic nano-thin polymer films. Demonstrations include extraction of modulus and density of coatings by use of multimodal resonances of a single, reusable measurement platform. Integrated thermal actuators allow for evaluation of the temperature dependence of the modulus, including those associated with phase transitions. Theoretical modeling and design suggest the potential for measurement of anisotropic mechanical properties in single or multilayer films.

RESULTS

3D Multimodal Vibratory Systems Actuated by Lorentz Force. Figure 1a is a schematic illustration of a representative 3D system assembled on an elastomeric substrate. The overall size, as measured by the distance between the two sites at which the structure bonds to the substrate, is 800 μm. The critical dimension, as defined by the width of the narrowest ribbon, is 100 μm. As shown by the exploded view in Figure 1b, this platform consists of a layer of patterned conductive traces (Au, thickness = 300 nm) sandwiched between two layers of polyimide (PI, thickness ∼2.5 μm for each). The PI layers not only form the structural components of the system but also encapsulate and protect the traces. The 3D architecture results from mechanical buckling of a 2D precursor (see Figure S1) *via* controlled release of a prestretched elastomeric substrate, as described elsewhere.[36−39] The detailed fabrication process for the precursors appears in Figure S2 and Methods. Briefly, layers of PI and gold are consecutively deposited on a silicon wafer and patterned using photolithography. Dissolution of a sacrificial layer of poly(methyl methacrylate) (PMMA) releases the precursor formed in this manner from the underlying wafer. The planar nature of the process then allows integration of nano-thin polymer films as test vehicles with a wide range of thicknesses and geometries. In this work, we demonstrate the use of a photodefinable epoxy (SU8), a cresol novolak resin (S1805), and a polymer brush (PNIPAm) as test films, patterned onto the 2D precursors *via* photopolymerization, photolithography, and selective growth, respectively (see Methods for details).

Figure 1c and Figure S3 highlight the systems for Lorentz-force actuation and optical measurement. The Lorentz force follows from use of a sinusoidal voltage source (1.5 V, Keithley 3390) to create an alternating current (AC) through the traces, with a permanent magnet (neodymium disc) placed underneath the 3D structure to induce a static magnetic field in the z-direction. The result is an AC oscillatory force at the frequency of the current, imparted onto the traces at a direction perpendicular to the current and the magnetic field. The amplitude of the Lorentz force can be estimated by $F = B \times I_{rms} \times L_{Au} \approx 12.5\ \mu$N (magnetic field ($B$) ≈ 0.5T; rms value of electric current (I_{rms}) = 25 mA; gold wire length (L_{Au}) = 1 mm). The optical measurement system uses apparatus reported in previous work[30] based on lock-in detection of laser light scattered from the 3D structure. The amplitude of such a measurement is approximately proportional to the amplitude of the vibration. Additional details are in Methods. Changing the position of the magnet alters the direction of the magnetic field to allow actuation of targeted vibration modes. Figure 1d illustrates the lowest in-plane and out-of-plane vibration modes, obtained by 3D finite element analysis (FEA, see SI Section S1 for details). Experimentally, these modes are excited by placing the magnet below (denoted as mode 1, Figure S4a) and to the left of the 3D structure (denoted as mode 2, Figure S4b), respectively.

Characterization of Modulus and Density Using Multimodal Resonances. The effects of the patterned nano-thin polymer films under test on the vibrational frequencies of these two modes allow determination of both the modulus and density of the same sample. Dimensional analysis (see SI Section S2 for details) and FEA suggest a linear relationship between the resonant frequency and the polymer modulus and density:

$$\frac{f}{f_0} = C_E \frac{E_P h_P}{\hat{E}_{Base} h_{Base}} - C_\rho \frac{\rho_P h_P}{\hat{\rho}_{Base} h_{Base}} \quad (1)$$

where f and f_0 are the resonant frequencies with and without the polymer, E_P, ρ_P, and h_P are the polymer modulus, density, and thickness, $\hat{E}_{Base}$, $\hat{\rho}_{Base}$, and h_{Base} are the effective modulus, average density, and thickness of the PI/Au/PI trilayer, respectively (see SI Section S3 for details), and the dimensionless parameters C_E and C_ρ depend on the topology of the 3D vibratory platform, the vibration mode, and the geometries of nano-thin polymer patterns and gold circuits. For the 3D structure, vibration modes and nano-thin polymer/gold patterns in Figure S5, FEA gives $C_{E(1)} = 0.44$, $C_{\rho(1)} = 0.30$ for mode 1 and $C_{E(2)} = 0.20$, $C_{\rho(2)} = 0.30$ for mode 2, as shown in Figure 2a,b. The results indicate that the specific designs of the nano-thin polymer patterns and the vibration modes enable partial decoupling of the sensitivities of resonant frequencies to the polymer modulus and density. In particular, the resonant frequency of mode 1 is 2.2 ($C_{E(1)}/C_{E(2)}$) times more sensitive to the polymer modulus than that of mode 2, as measured by the slope of the curves in Figure 2a. Meanwhile the resonant frequencies of both modes are sufficiently sensitive to the polymer density. The design of the nano-thin polymer

DOI: 10.1021/acsnano.8b06736
ACS Nano 2019, 13, 449−457

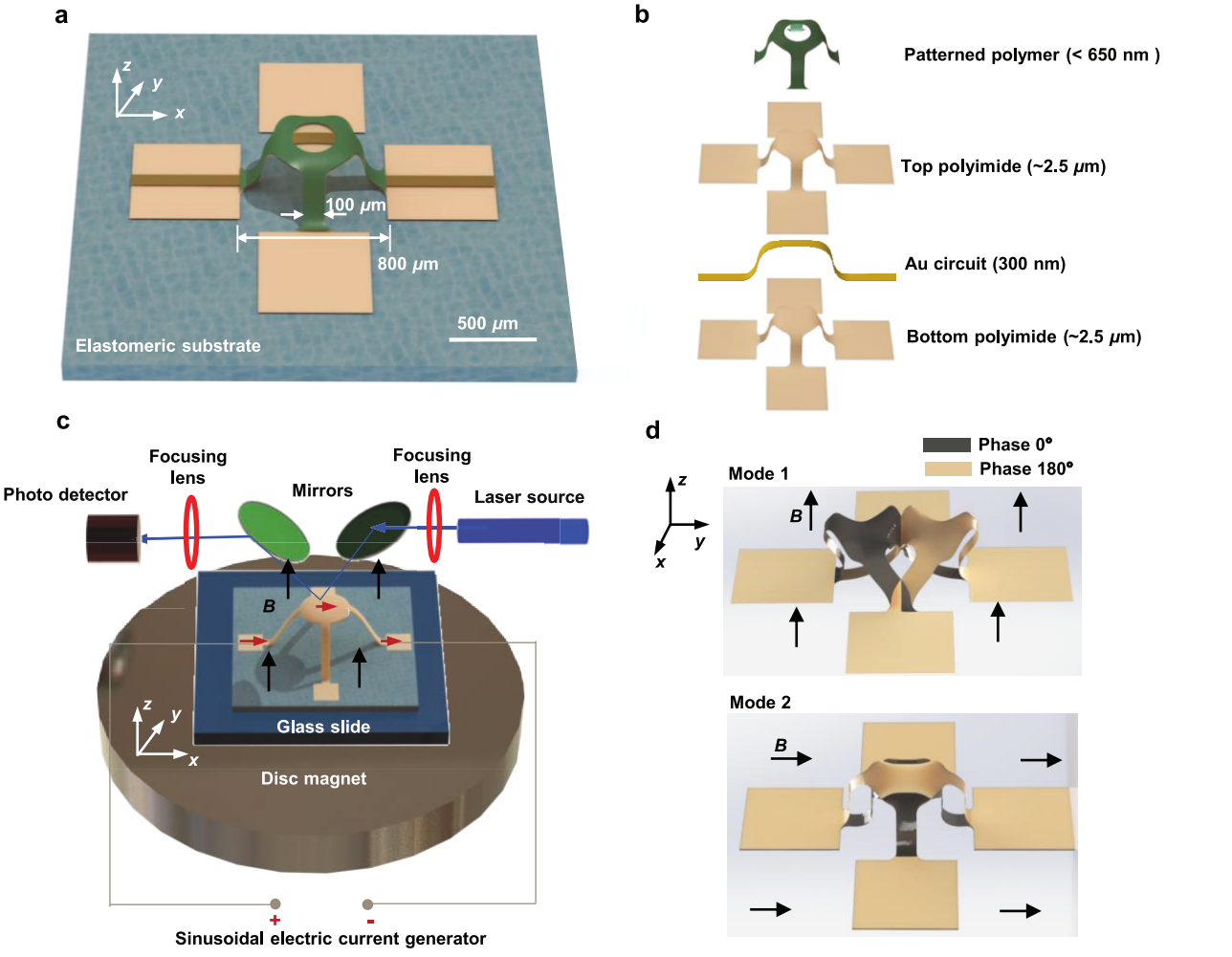

Figure 1. 3D microstructure actuated by Lorentz force. (a) Schematic illustrations of the 3D structure, assembled on an elastomer substrate. (b) Exploded view of the layered composition with integrated conductive traces. (c) Schematic illustration of the measurement system, consisting of a magnet and current source for Lorentz-force actuation and a laser apparatus for detection of vibrational motions. (d) FEA views of the two distinct vibration modes of the vibrator, achieved by placing the permanent magnet at the bottom (top frame) and at the side (bottom frame). The amplitudes of the vibrations are exaggerated for viewing purposes.

patterns follows from use of a FEA-based algorithm that optimizes the contribution of the polymer to the strain energy and the kinetic energy of the vibrations (see SI Section S4 for details). The developed scaling law serves as the basis of an inverse problem to determine the polymer tensile stiffness ($E_P h_P$) and mass ($\rho_P h_P$) from the measured resonant frequencies (see SI Section S5 for details).

In principle, the method is applicable to evaluation of any type of material (polymers, metals, ceramics), but the tensile stiffness ($E_P h_P$) and mass ($\rho_P h_P$) of the films must be at least 1 order of magnitude smaller than those of the base layer ($\hat{E}_{Base} h_{Base}$ = 1.36×10^4N/m and $\hat{\rho}_{Base} h_{Base}$ = 0.013 kg/m^2 for the design shown in Figure 2a), such that the linear relationship in eq 1 applies. For all the polymers studied in this paper, $E_{Base} \approx E_P$ and $\rho_{Base} \approx \rho_P$, so h_P should be approximately 1 order of magnitude smaller than h_{Base}. h_{Base} in Figure 2a is on the order of 10 μm, which can be used to measure nano-thin films with h_P on the order of 10^2 nm or smaller. In such cases, to deduce the elastic modulus (E_P) and density (ρ_P) of the polymer from multimodal frequency measurements, the thickness (h_P) of the nano-thin polymer film must be known. Measurements of thickness are most easily performed prior to 3D assembly, in the precursor 2D geometry with techniques such as surface profilometry or spectroscopic ellipsometry (see Methods for details), with uncertainty of ~5%.

As an example, Figure 2c,d shows experimental measurements of the response curves of modes 1 and 2, respectively, for the case of a patterned nano-thin layer of a photodefinable epoxy (SU8; thickness = 610 nm, Figure S6b). The resonant frequencies are $f_{(1)}$ = 30.6 kHz, $f_{0(1)}$ = 28.8 kHz for mode 1, and $f_{(2)}$ = 28.4 kHz, $f_{0(2)}$ = 27.9 kHz for mode 2. The repeatability of the measurement is ~0.1%, as defined by the standard deviation of four measurements performed in sequence (Figure S7). The effective modulus, average density, and thickness of the base layer are $\hat{E}_{Base}$ = 2.51 GPa, $\hat{\rho}_{Base}$ = 2.41 g/cm^3, and h_{Base} = 5.4 μm, respectively. Inserting these values into eq 1 yields the modulus E_P = 3.8 ± 0.4 GPa and density ρ_P = 1.3 ± 0.3 g/cm^3 of the epoxy, as presented in Figure 2e. The combined uncertainties in thickness and frequency lead to ~10% and ~20% uncertainties in the extracted film modulus and density, respectively (see SI Section S5 for details). The ~5% discrepancies between the modulus and density values reported here and those in the literature (SU8 modulus 4.02 GPa; SU8 density 1.22 g/cm^3) are within the uncertainties.

Based on the theoretical model (eq 1 and eqs S10–S12), both the relative uncertainties in the as determined polymer modulus

DOI: 10.1021/acsnano.8b06736
ACS Nano 2019, 13, 449–457

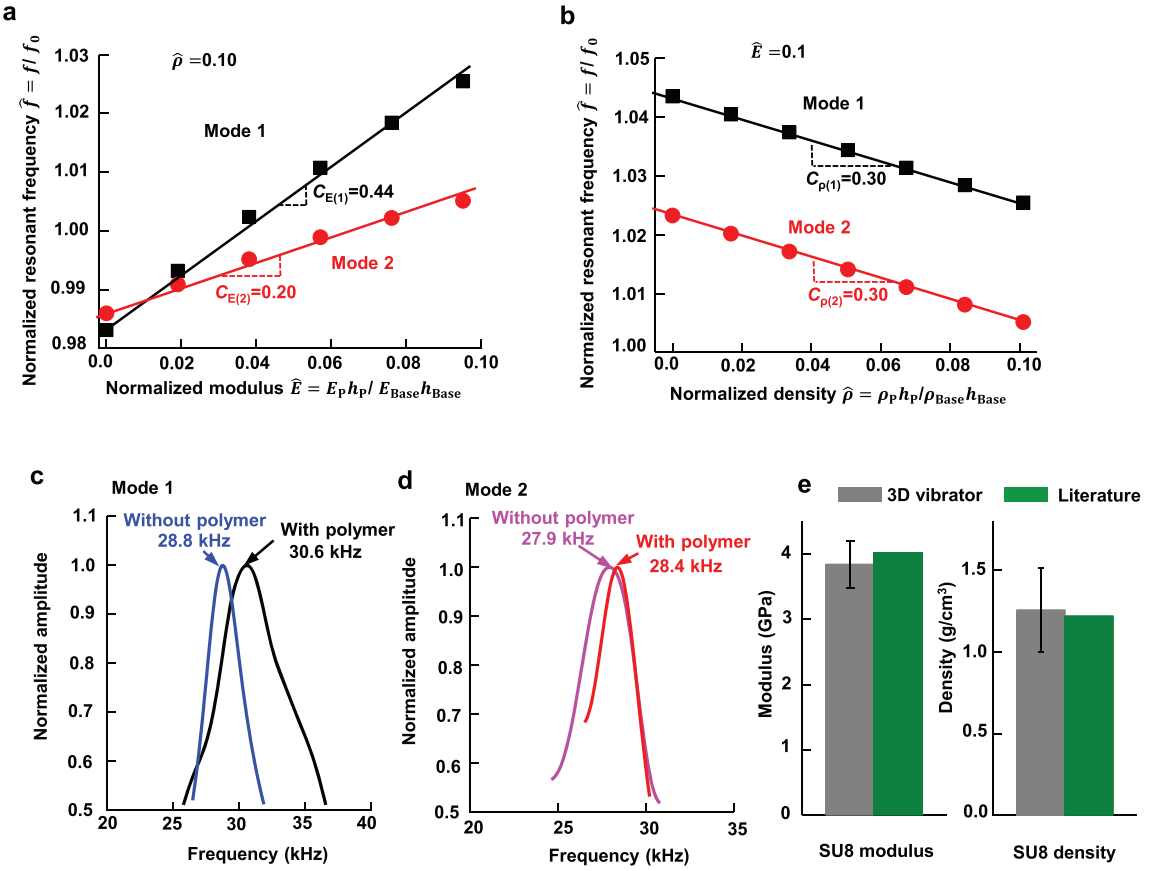

Figure 2. Measurement of modulus and density using a single 3D microstructure. (a, b) FEA results for variation of the normalized resonant frequency with the normalized modulus (a) and the normalized density (b), for both vibration modes 1 and 2. (c, d) Measurement results of the normalized amplitude *versus* frequency for mode 1 (c) and mode 2 (d). (e) Modulus (left frame) and density (right frame) determined by the 3D vibratory structure, compared with the literature values.

($\frac{\delta E_P}{E_P}$) and density ($\frac{\delta \rho_P}{\rho_P}$) depend linearly on the uncertainties in the measured resonant frequency (δf, see Figure S8 for details). Park *et al.* reports that using the laser Doppler vibrometer (MSV-300, Polytec), the uncertainty in the resonant frequency can be reduced to 1 Hz when the resonant frequency is on the order of $10-10^2$ kHz,[40] that is, δf = 1 Hz. With such a level of precision, the relative uncertainties in the as determined polymer modulus and density can be reduced to 0.25% and 0.87%, respectively. The relative uncertainty in the thickness measurement, on the other hand, is also linearly related to the uncertainties in the as determined modulus and density. For example, a 1% reduction in uncertainty in the thickness measurement corresponds to a 1% reduction in uncertainty in the as determined polymer modulus and density.

Robustness and Reusability of 3D Vibrators. The elastic, reversible nature of the 3D assembly process allows repetitive use of these measurement platforms. Specifically, after measuring one nano-thin polymer sample, applying tensile strain on the underlying elastomeric substrate fully returns the 3D structure to its unbuckled, 2D form, thus allowing the removal of the nano-thin film under test and application of another material (see Figure S9 for the schematic illustration). Release of the tensile strain reassembles the 3D structure for frequency measurements. Cycling tests that involve 500 cycles of stretching/release reveal a resonance frequency shift of <0.3% (from 34.90 ± 0.03 kHz to 35.00 ± 0.03 kHz), despite an increase in circuit resistance of ~20% (Figure S10) perhaps due to some level of plastic yielding in the gold layer. Because the gold (300 nm) is much thinner than the PI (~5 μm) and because it is positioned at the neutral mechanical plane, its plastic yielding has a minor effect on the overall resonant frequency. As a demonstrating example, Figure 3b shows a set of experimental results on two cresol novolak resin (S1805) nano-thin films with different thicknesses (450 ± 30 nm and 650 ± 40 nm), actuated with mode 1. The scanning electron microscope images of the device before and after the novolak resin is spin coated (Figure S11) indicate full coverage and good uniformity of the resulted film. Note that after washing away S1805 with acetone, the response curve of the 3D vibrator matches the initial polymer-free state exceptionally well, indicating good robustness and repeatability of the system as well as effectively complete removal of S1805.

Integration with Thermal Actuators for Temperature-Dependent Measurements. The compatibility with planar fabrication technologies allows integration of additional actuating and sensing elements, *via* a few additional fabrication steps (see Methods for fabrication details). As a specific example, thermal actuators allow studies of modulus as a function of temperature. Figure 4a shows schematic illustrations of a modified 3D platform that includes this functionality. A bilayer of photodefinable epoxy (SU8, thickness = 40 ± 2 nm) and a poly(*N*-isopropylacrylamide) (PNIPAm) brush (thickness = 270 ± 20 nm) patterned directly on top of the thermal actuators serve as the test sample (see Methods for experimental details). Figure 4b shows the FEA calibration of the temperature change

DOI: 10.1021/acsnano.8b06736
ACS Nano 2019, 13, 449−457

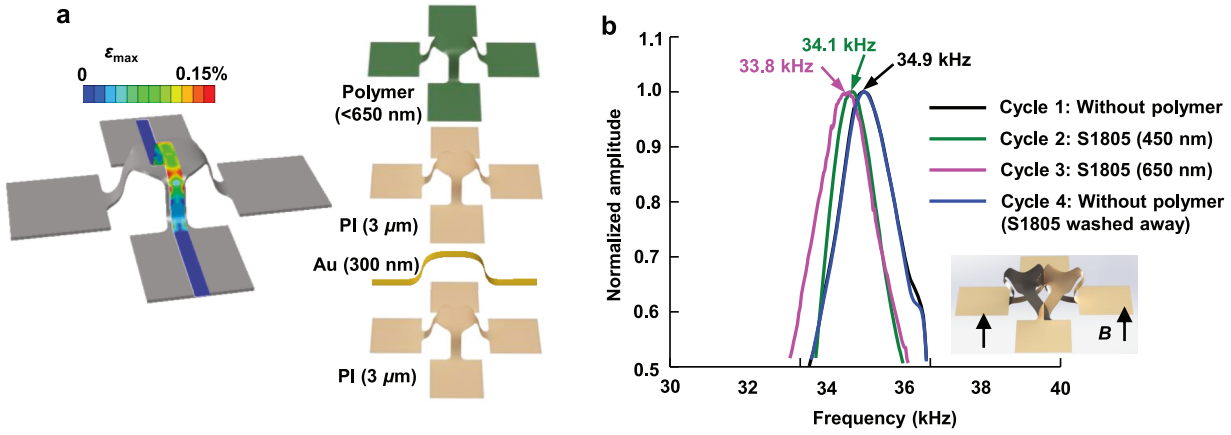

Figure 3. Reusability of the 3D vibratory structure. (a) Maximum strain in the gold layer obtained by FEA, which is below its yield strain (left frame). Exploded view of the layered composition of the vibratory platform (right frame). (b) FEA views of the vibration mode in this measurement (inset), and a series of measurement results on the same platform using different testing subjects. The amplitudes of the vibrations are exaggerated for viewing purposes.

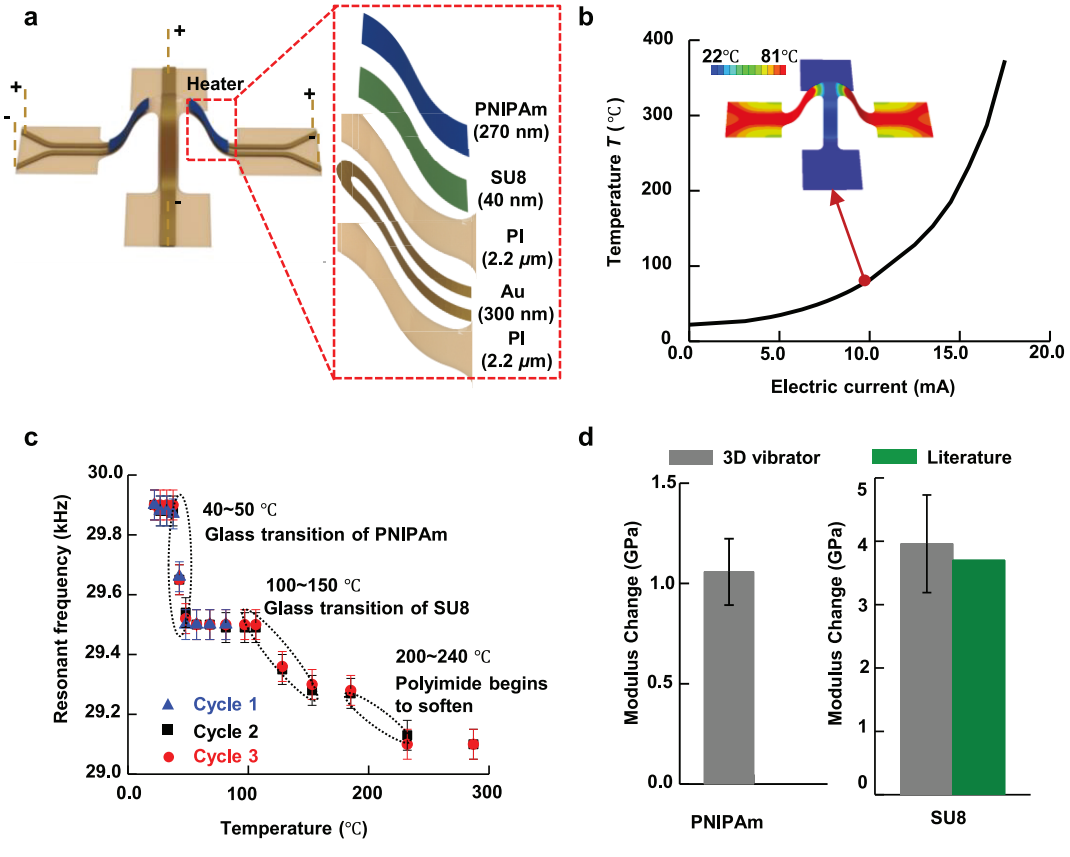

Figure 4. 3D vibratory platform integrated with thermal actuators. (a) Schematic illustration of the 3D architecture integrated with thermal actuators, circuits for Lorentz-force actuation and patterned polymer film (left frame), and magnified, exploded view of the section containing the thermal actuators (right frame). (b) Calibration of temperature *versus* supplied electric current. (c) Experimental results for the variation of the resonant frequency with temperature. (d) Change in modulus of PNIPAm (left frame) and SU8 (right frame) determined from the results in (c).

versus direct current input for the thermal actuator (see SI Section S1 for details).[41] The temperature change at the nano-thin polymer region is uniform, as illustrated by the inset of Figure 4b. The experimental results in Figure 4c show as expected that the resonant frequency decreases as the temperature increases. Measurements for three cycles of heating are in Figure 4c, where the peak temperature is 80 °C in the nano-thin polymer in cycle 1 (denoted by the blue solid triangles) and 300 °C in cycles 2 (red solid circles) and 3 (black solid squares). The sharp, ~0.5 ± 0.05 kHz decrease in resonant frequency at 40−50 °C corresponds to the glass transition of PNIPAm, while the ~0.2 ± 0.05 kHz decrease at 100−150 °C corresponds to that of SU8. The measured glass transition temperature matches well with the literature values for SU8,[42] whereas it is lower than the reported values for bulk PNIPAm,[43] as expected for this material which contains short polymer chain lengths and has a small thicknesses.[44−49] During the glass transition, the change in polymer mass ($\rho_P h_P$) is negligible because of mass

DOI: 10.1021/acsnano.8b06736
ACS Nano 2019, 13, 449−457

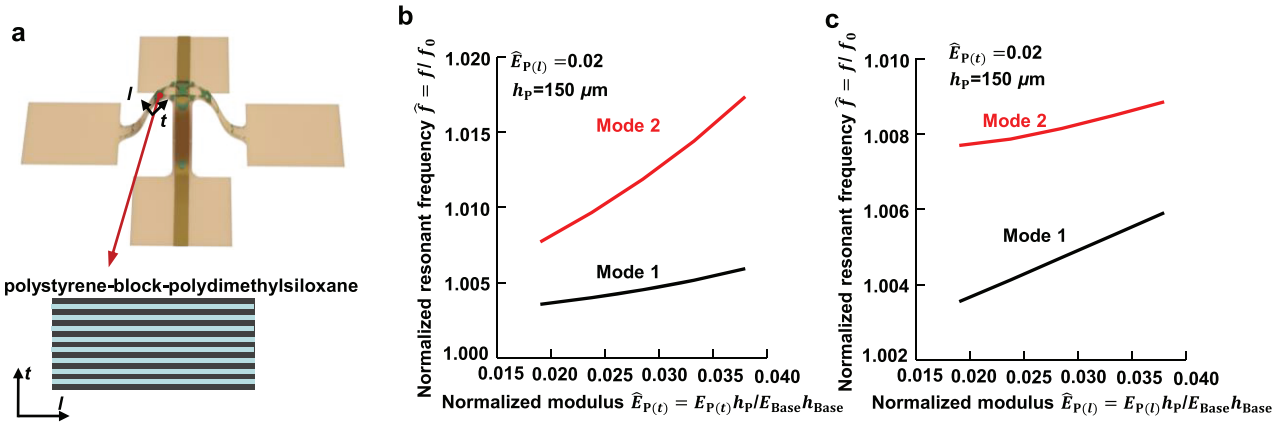

Figure 5. Theoretical investigation of measurement of anisotropic elastic moduli using a 3D vibratory platform. (a) Schematic illustration of the 3D vibratory platform with a thin film that has anisotropic elastic moduli. In this case, the thin film has different elastic moduli along the transverse (t) and longitudinal (l) directions. (b, c) FEA results of normalized resonant frequency for mode 1 and mode 2 with normalized modulus in transverse (t) (b) and longitudinal (l) (c) directions, respectively.

conservation; the change in polymer thickness is also small (<1%) due to the small coefficient of thermal expansion[50,51] and the small change in temperature across the glass transition. The changes in the moduli of PNIPAm and SU8 nano-thin films are thus determined from the corresponding resonant frequency shifts to be $\Delta E_{PNIPAm} = 1.1 \pm 0.2$ GPa and $\Delta E_{SU8} = 4 \pm 1$ GPa, respectively (Figure 4d, see SI Section S6 for detailed calculations). The difference between the measured change in modulus of SU8 across the glass transition is consistent with the literature value (3.7 GPa),[42] to within experimental uncertainties. Finally, the further reduction in resonant frequency above 200 °C is likely attributable to the onset of softening of PI itself.[52]

Potential for Characterization of Anisotropic Elastic Moduli Using Multimodal Resonances. The multimodal resonances of the 3D structures and the ability to pattern nano-thin polymers in a precise manner provide routes to determine the elastic moduli of anisotropic materials. Figure 5 presents schematic illustrations of the 3D vibratory structure with patterned test films that have transversely isotropic elastic moduli (for instance, oriented polystyrene-*block*-polydimethylsiloxane films).[53] The optimized patterns are shown in Figure S12, with the optimization algorithm presented in the SI Section S4. Briefly, the optimization algorithm uses FEA results for the distributions of strain components. To enhance the sensitivity of the resonant frequencies to the longitudinal component of the modulus, the test polymer should be patterned in locations with the largest strain along the longitudinal direction. The same consideration holds true for the transverse modulus component. Optimized patterns of typical polymers balance these two considerations (see SI Section 4 for details). For the current design, the resonant frequency of mode 2 is roughly 2.5 times more sensitive to the transverse modulus ($E_{P(t)}$) than the mode 1 (Figure 5b), while the latter is roughly 1.5 times more sensitive to the longitudinal modulus ($E_{P(l)}$, see Figure 5c) than the former, as measured by the slopes of the curves in Figure 5b,c. This decoupling allows determination of both the longitudinal and transverse moduli by measuring the frequency of modes 1 and 2 with and without the nano-thin polymer patterns, provided that the polymer density and thickness are known.

CONCLUSIONS

In summary, the results presented here demonstrate the applicability of 3D vibratory platforms to characterize the properties of nano-thin film materials, with demonstrations on three different types of polymers. With the current device parameters and optical measurement setups, modulus and density of any thin film with sufficiently small tensile stiffness and mass can be reliably and independently measured on the same sample. The robustness and reusability of these 3D systems, together with their utility in evaluating temperature-dependent film properties, create a broad range of possible uses. Theoretical modeling and design suggest opportunities for measuring anisotropic materials properties, specifically the transverse isotropic moduli of thin films. The assembly approaches can be applied to 3D structures with reduced dimensions, increased operating frequencies, and enhanced sensitivity.

METHODS

Fabrication of 3D Vibratory Platforms. Fabrication began with spin coating a bilayer of poly(methyl methacrylate) (950 PMMA A4, MicroChem, thickness ~200 nm) and polyimide (PI 2545, HD MicroSystems, thickness ~2.5 μm) on a silicon wafer. Depositing Cr (thickness ~5 nm) and Au (thickness ~300 nm) by electron beam evaporation followed by photolithography and wet etching defined the circuits. Spin coating another layer of PI (thickness ~2.5 μm) followed by deposition and patterning of Cr (thickness ~5 nm) and Au (thickness ~50 nm) defined a hard mask in the shape of 2D devices, where the external electrodes were exposed for connections with the function generator. Oxygen plasma etching (March Jupiter III RIE) removes the unmasked PI. After removing the etching mask by wet etching, a layer of polymer was patterned on top to serve as the measurand (see below for details). The underlying PMMA layer was dissolved by immersion in acetone overnight to allow retrieval of the device onto a piece of water-soluble tape. A thin layer of silicon oxide (thickness ~50 nm) deposited on the back side of the sample by electron beam evaporation created the necessary surface chemistry for strong adhesion to the elastomer platform at the bonding sites. The nonbonding sites were protected from SiO_2 deposition by a Kapton shadow mask created by laser cutting. A silicone elastomeric substrate (Dragon Skin 10) was stretched to a desired prestrain (30–40%) using a customized, biaxial stage. After exposing the elastomer and the 2D precursors (still on water-soluble tape) to ultraviolet (UV) induced ozone (Jelight UVO-Cleaner, Model 144AX), the two were laminated together and then baked in a convection oven at 70 °C to yield strong adhesion at the bonding sites where SiO_2 was deposited. Finally, dissolving the tape in warm water and slowly releasing the prestrain completed the assembly process. A schematic illustration of the procedures can be found in Figure S2.

Patterning and Characterizing the Thicknesses of the Polymer Films. Patterning the SU8 film used in Figure 2 began

DOI: 10.1021/acsnano.8b06736
ACS Nano 2019, 13, 449–457

with spin coating the SU8 precursor (SU8 2000.5, MicroChem) onto the 2D devices at 2000 rpm for 40 s. After prebaking at 95 °C for 1 min, the film was exposed under an iron oxide photomask with 365 nm UV light at an intensity of 60 mJ/cm^2. Post-exposure baking at 95 °C for 1 min and developing in SU8 developer (MicroChem) yielded the desired patterns on the 2D precursors. The sample was then hard baked at 200 °C for 10 min. The thickness was characterized using a profilometer (Dektak 3030), while the 2D precursors were still on the silicon wafer.

Patterning of the S1805 films used in Figure 3 began by forming the 3D vibratory platforms, as described in the previous section, and stretching the elastomeric substrate to fully recover its 2D form. After rinsing the sample with acetone, isopropanol alcohol, and DI water, the S1805 precursor (MicroChem) was spin coated at 4000 rpm (cycle 2, Figure 3b) or 2000 rpm (cycle 3, Figure 3c), followed by baking at 110 °C for 3 min. The elastomeric substrate was then relaxed to return the sample to its 3D form. After each cycle, the sample was thoroughly rinsed with acetone to completely remove the S1805 film.

Patterning of the bilayer of SU8 and poly(*N*-isopropylacrylamide) (PNIPAm) brush used in Figure 4 began by spin coating SU8 precursor (SU8 2002, MicroChem), diluted using cyclopentanone with a 1:5 volume ratio, onto the 2D devices at 4000 rpm for 40 s. After prebaking at 95 °C for 1 min, the film was exposed under an iron oxide photomask with 365 nm UV light at an intensity of 50 mJ/cm^2. Post-exposure baking at 95 °C for 1 min and developing in SU8 developer (MicroChem) defined the desired patterns on the 2D precursors. The sample was then hard baked at 200 °C for 10 min. The PNIPAm brush was selectively grown on the SU8 patterns using surface-initiated atom-transfer radical polymerization (SI-ATRP) using previously reported procedures. Briefly, SU8 surfaces were activated using oxygen plasma for 3 min (150 W, March Plasmod GCM-200) and then functionalized with the ATRP initiator (11-(2-bromo-2-methyl)propionyloxy) undecyltrichlorosilane (BMPOUTS). Devices were placed in a 1 mM solution of BMPOUTS in anhydrous hexanes at room temperature. After 24 h, substrates were removed, sonicated in hexanes, dried using a nitrogen stream, and placed in a reaction vessel under argon. NIPAM (4.85 g, 42.9 mmol) was diluted with MeOH (15 mL) and H_2O (7 mL) and degassed in a separate Schlenk flask. Then, 1,1,4,7,10,10-hexamethyltriethylenetetramine (HMTETA, 242 μL, 0.89 mmol) and CuBr (53.8 mg, 0.38 mmol) were added to the monomer solution under positive argon flow. Once dissolved, the flask was then sealed, and the mixture was transferred to the reaction vessel containing the substrates. Substrates were removed after 10 min, sonicated in methanol, ethanol, and water to remove the film residuals in the non-SU8 regions, and then dried in a nitrogen stream.

The thickness of the PNIPAm brush was determined using spectroscopic ellipsometry (VASE, J.A. Wollam Co) on a control sample. Ellipsometric parameters (Ψ, Δ) were measured at three angles of incidence (65°, 70°, 75°) and from 400 to 800 nm. Data were analyzed by WVASE software using a three-layer model. Software-supplied refractive indices were used for silicon (substrate) and silicon dioxide (2 nm). Data were fit to a Cauchy layer model, with fixed (An, Bn) values of (1.45, 0.01) and no optical absorption. Control samples were prepared by growing the PNIPAm brush off a silicon wafer that had been patterned with SU8 using the identical conditions as the actual samples. The SU8 layer was determined to be 39.6 nm. After polymerization, the total thickness of the polymer layers (SU-8 and PNIPAM) was determined to be 312.9 nm. Thus, the NIPAM brush thickness is approximately 273.3 nm.

Lorentz-Force Actuation System and Optical Measurement System. A function generator (Keithley 3390) applied 1.5 V sinusoidal voltage to the 3D vibratory structure while placed in a static magnetic field induced by a permanent neodymium disc magnet. The Lorentz force, perpendicular to both the electric current and the magnetic field, oscillated at the frequency of the applied voltage to drive vibrations of the structure.

An optical measurement system was custom-built to measure the dynamics of the 3D vibratory platforms (Figure S3). A focusing lens and mirror delivered a focused laser beam onto the center of the 3D structure. A microscope facilitated alignment. The 3D structure was firmly mounted onto a mechanical stage capable of translation in *X*-, *Y*-, and *Z*-directions and tilt with respect to *X*- and *Y*-axes. Light scattered from the 3D structure was reflected by a second mirror, collected by a second lens and directed to a photodetector (Thorlabs, DET110) for intensity measurements. The fluctuations in the scattering intensity due to the 3D vibrations generated photocurrent in the photodetector with the same overall time dependence. The system was tuned such that the amplitude of the photocurrent responded linearly to the amplitude of the input voltage. Within the operational range of frequency, the amplitude of the fluctuating photocurrent is directly proportional to the vibration amplitude, which peaked at the resonant frequency. A lock-in amplifier (SRS 830, Stanford Research Systems) was used to record the amplitude of the photocurrent.

A Labview program was used to sweep the desired range of frequency and convert data from the lock-in amplifier. At each frequency, the measurement was repeated 64 times to ensure minimum fluctuations, and the increment of frequency was 50 Hz. The error of the system was determined to be ∼50 Hz.

ASSOCIATED CONTENT

Supporting Information

The Supporting Information is available free of charge on the ACS Publications website at DOI: 10.1021/acsnano.8b06736.

Section S1, Finite element analysis (FEA). Section S2, The scaling law in eq 1. Section S3, Effective modulus and average density of an *n*-layer composite. Section S4, Algorithm that optimizes the polymer patterns. Section S5, Determination of the polymer modulus and density from the resonant frequency of two vibration modes. Section S6, Determination of the polymer tensile stiffness change during glass transition Figures S1−S12 (PDF)

AUTHOR INFORMATION

Corresponding Authors

*E-mail: pbraun@illinois.edu.
*E-mail: jrogers@northwestern.edu.
*E-mail: y-huang@northwestern.edu.

ORCID

Kewang Nan: 0000-0002-2745-0656
Yihui Zhang: 0000-0003-0885-2067
Paul V. Braun: 0000-0003-4079-8160

Author Contributions

◆These authors contributed equally.

Notes

The authors declare no competing financial interest.

ACKNOWLEDGMENTS

All experimental efforts presented were supported by the U.S. Department of Energy, Office of Basic Energy Sciences, Division of Materials Sciences and Engineering under award no. DE-FG02-07ER46471, through the Frederick Seitz Materials Research Laboratory at the University of Illinois at Urbana−Champaign. K.A.M. was supported by National Science Foundation Graduate Research Fellowship Program under grant no. DGE 1746047. Y.Z. acknowledged the support from the National Natural Science Foundation of China (11722217) and the Tsinghua National Laboratory for Information Science and Technology. Y.H. acknowledged the support from NSF (nos. CMMI1400169, CMMI1534120, and CMMI1635443). Y.X. acknowledged the support from the Ryan Fellowship and the Northwestern University International Institute for Nanotechnology.

DOI: 10.1021/acsnano.8b06736
ACS Nano 2019, 13, 449−457

REFERENCES

(1) Jensen, K.; Kim, K.; Zettl, A. An Atomic-Resolution Nanomechanical Mass Sensor. *Nat. Nanotechnol.* **2008**, *3*, 533−537.

(2) Yang, Y. T.; Callegari, C.; Feng, X. L.; Ekinci, K. L.; Roukes, M. L. Zeptogram-Scale Nanomechanical Mass Sensing. *Nano Lett.* **2006**, *6*, 583−586.

(3) Chaste, J.; Eichler, A.; Moser, J.; Ceballos, G.; Rurali, R.; Bachtold, A. A Nanomechanical Mass Sensor with Yoctogram Resolution. *Nat. Nanotechnol.* **2012**, *7*, 301−304.

(4) Xiong, Q.; Duarte, N.; Tadigadapa, S.; Eklund, P. C. Force-Deflection Spectroscopy: A New Method to Determine the Young's Modulus of Nanofilaments. *Nano Lett.* **2006**, *6*, 1904−1909.

(5) Christopher, G. F.; Yoo, J. M.; Dagalakis, N.; Hudson, S. D.; Migler, K. B. Development of a MEMS Based Dynamic Rheometer. *Lab Chip* **2010**, *10*, 2749−2757.

(6) Zhang, X. C.; Myers, E. B.; Sader, J. E.; Roukes, M. L. Nanomechanical Torsional Resonators for Frequency-Shift Infrared Thermal Sensing. *Nano Lett.* **2013**, *13*, 1528−1534.

(7) Choi, W. J.; Jeon, Y.; Jeong, J. H.; Sood, R.; Kim, S. G. Energy Harvesting MEMS Device Based on Thin Film Piezoelectric Cantilevers. *J. Electroceram.* **2006**, *17*, 543−548.

(8) Liu, J.-Q.; Fang, H.-B.; Xu, Z.-Y.; Mao, X.-H.; Shen, X.-C.; Chen, D.; Liao, H.; Cai, B.-C. A MEMS-Based Piezoelectric Power Generator Array for Vibration Energy Harvesting. *Microelectron. J.* **2008**, *39*, 802−806.

(9) Fang, H.-B.; Liu, J.-Q.; Xu, Z.-Y.; Dong, L.; Wang, L.; Chen, D.; Cai, B.-C.; Liu, Y. Fabrication and Performance of MEMS-Based Piezoelectric Power Generator for Vibration Energy Harvesting. *Microelectron. J.* **2006**, *37*, 1280−1284.

(10) Yang, S.; Zhao, X.; Sharma, P. Avoiding the Pull-in Instability of a Dielectric Elastomer Film and the Potential for Increased Actuation and Energy Harvesting. *Soft Matter* **2017**, *13*, 4552−4558.

(11) Alameh, Z.; Yang, S.; Deng, Q.; Sharma, P. Emergent Magnetoelectricity in Soft Materials, Instability, and Wireless Energy Harvesting. *Soft Matter* **2018**, *14*, 5856−5868.

(12) Yao, S.; Myers, A.; Malhotra, A.; Lin, F.; Bozkurt, A.; Muth, J. F.; Zhu, Y. A Wearable Hydration Sensor with Conformal Nanowire Electrodes. *Adv. Healthcare Mater.* **2017**, *6*, 1601159.

(13) Yao, S.; Swetha, P.; Zhu, Y. Nanomaterial-Enabled Wearable Sensors for Healthcare. *Adv. Healthcare Mater.* **2018**, *7*, 1700889.

(14) Shian, S.; Bertoldi, K.; Clarke, D. R. Dielectric Elastomer Based "Grippers" for Soft Robotics. *Adv. Mater.* **2015**, *27*, 6814−6819.

(15) Kumar, K.; Liu, J.; Christianson, C.; Ali, M.; Tolley, M. T.; Aizenberg, J.; Ingber, D. E.; Weaver, J. C.; Bertoldi, K. A Biologically Inspired, Functionally Graded End Effector for Soft Robotics Applications. *Soft Robot.* **2017**, *4*, 317−323.

(16) Dufour, I.; Maali, A.; Amarouchene, Y.; Ayela, C.; Caillard, B.; Darwiche, A.; Guirardel, M.; Kellay, H.; Lemaire, E.; Mathieu, F.; Pellet, C.; Saya, D.; Youssry, M.; Nicu, L.; Colin, A. The Microcantilever: A Versatile Tool for Measuring the Rheological Properties of Complex Fluids. *J. Sens.* **2012**, *2012*, 719898.

(17) Belov, M.; Quitoriano, N. J.; Sharma, S.; Hiebert, W. K.; Kamins, T. I.; Evoy, S. Mechanical Resonance of Clamped Silicon Nanowires Measured by Optical Interferometry. *J. Appl. Phys.* **2008**, *103*, No. 074304.

(18) Seo, J. H.; Brand, O. High Q-Factor in-Plane-Mode Resonant Microsensor Platform for Gaseous/Liquid Environment. *J. Microelectromech. Syst.* **2008**, *17*, 483−493.

(19) Menzel, A.; Waffenschmidt, T. A Microsphere-based Remodeling Formulation for Anisotropic Biological Tissues. *Philos. Trans. R. Soc., A* **2009**, *367*, 3499−3523.

(20) *Mechanics of Biological Tissue*; Holzapfel, G. A.; Ogden, R. W., Eds.; Springer-Verlag: Berlin, 2006.

(21) Gennisson, J. L.; Deffieux, T.; Macé, E.; Montaldo, G.; Fink, M.; Tanter, M. Viscoelastic and Anisotropic Mechanical Properties of *in vivo* Muscle Tissue Assessed by Supersonic Shear Imaging. *Ultrasound Med. Bio.* **2010**, *36*, 789−801.

(22) Tan, J. C.; Merrill, C. A.; Orton, J. B.; Cheetham, A. K. Anisotropic Mechanical Properties of Polymorphic Hybrid Inorganic−Organic Framework Materials with Different Dimensionalities. *Acta Mater.* **2009**, *57*, 3481−3496.

(23) Kim, G. H. Electrospun PCL Nanofibers with Anisotropic Mechanical Properties as a Biomedical Scaffold. *Biomed. Mater.* **2008**, *3*, No. 025010.

(24) Haque, M. A.; Kamita, G.; Kurokawa, T.; Tsujii, K.; Gong, J. P. Unidirectional Alignment of Lamellar Bilayer in Hydrogel: One-Dimensional Swelling, Anisotropic Modulus, and Stress/Strain Tunable Structural Color. *Adv. Mater.* **2010**, *22*, 5110−5114.

(25) Minnich, A. J. Phonon Heat Conduction in Layered Anisotropic Crystals. *Phys. Rev. B: Condens. Matter Mater. Phys.* **2015**, *91*, No. 085206.

(26) Minnich, A. J. Exploring the Extremes of Heat Conduction in Anisotropic Materials. *Nanoscale Microscale Thermophys. Eng.* **2016**, *20*, 1−21.

(27) Wang, Z.; Lee, J.; He, K.; Shan, J.; Feng, P. X. L. Embracing Structural Nonidealities and Asymmetries in Two-Dimensional Nanomechanical Resonators. *Sci. Rep.* **2015**, *4*, 3919−3926.

(28) Moore, S. I.; Ruppert, M. G.; Yong, Y. K. Multimodal Cantilevers with Novel Piezoelectric Layer Topology for Sensitivity Enhancement. *Beilstein J. Nanotechnol.* **2017**, *8*, 358−371.

(29) Ilic, B.; Krylov, S.; Craighead, H. G. Young's Modulus and Density Measurements of Thin Atomic Layer Deposited Films Using Resonant Nanomechanics. *J. Appl. Phys.* **2010**, *108* (4), No. 044317.

(30) Ning, X.; Wang, H.; Yu, X.; Soares, J. A.; Yan, Z.; Nan, K.; Velarde, G.; Xue, Y.; Sun, R.; Dong, Q.; Luan, H.; Lee, C. M.; Chempakasseril, A.; Han, M.; Wang, Y.; Li, L.; Huang, Y.; Zhang, Y.; Rogers, J. A. 3D Tunable, Multiscale, and Multistable Vibrational Micro-Platforms Assembled by Compressive Buckling. *Adv. Funct. Mater.* **2017**, *27*, 1605914.

(31) Wang, H.; Ning, X.; Li, H.; Luan, H.; Xue, Y.; Yu, X.; Fan, Z.; Li, L.; Rogers, J. A.; Zhang, Y.; Huang, Y. Vibration of Mechanically-Assembled 3D Microstructures Formed by Compressive Buckling. *J. Mech. Phys. Solids* **2018**, *112*, 187−208.

(32) Vinod, T. P.; Taylor, J. M.; Konda, A.; Morin, S. A. Stretchable Substrates for the Assembly of Polymeric Microstructures. *Small* **2017**, *13*, 1603350.

(33) Konda, A.; Rau, A.; Stoller, M. A.; Taylor, J. M.; Salam, A.; Pribil, G. A.; Argyropoulos, C.; Morin, S. A. Soft Microreactors for the Deposition of Conductive Metallic Traces on Planar, Embossed, and Curved Surfaces. *Adv. Funct. Mater.* **2018**, *28*, 1803020.

(34) Liao, X.; Xiao, J.; Ni, Y.; Li, C.; Chen, X. Self-Assembly of Islands on Spherical Substrates by Surface Instability. *ACS Nano* **2017**, *11*, 2611−2617.

(35) Ma, L.; Peng, J.; Wu, C.; He, L.; Ni, Y. Sphere-To-Tube Transition toward Nanotube Formation: A Universal Route by Inverse Plateau−Rayleigh Instability. *ACS Nano* **2017**, *11*, 2928−2933.

(36) Xu, S.; Yan, Z.; Jang, K. I.; Huang, W.; Fu, H.; Kim, J.; Wei, Z.; Flavin, M.; McCracken, J.; Wang, R.; Badea, A.; Liu, Y.; Xiao, D.; Zhou, G.; Lee, J.; Chung, H. U.; Cheng, H.; Ren, W.; Banks, A.; Li, X.; et al. Assembly of Micro/Nanomaterials into Complex, Three-Dimensional Architectures by Compressive Buckling. *Science* **2015**, *347*, 154−159.

(37) Zhang, Y.; Yan, Z.; Nan, K.; Xiao, D.; Liu, Y.; Luan, H.; Fu, H.; Wang, X.; Yang, Q.; Wang, J.; Ren, W.; Si, H.; Liu, F.; Yang, L.; Li, H.; Wang, J.; Guo, X.; Luo, H.; Wang, L.; Huang, Y.; Rogers, J. A. A Mechanically Driven Form of Kirigami as a Route to 3D Mesostructures in Micro/Nanomembranes. *Proc. Natl. Acad. Sci. U. S. A.* **2015**, *112*, 11757−11764.

(38) Zhang, Y.; Zhang, F.; Yan, Z.; Ma, Q.; Li, X.; Huang, Y.; Rogers, J. A. Printing, Folding and Assembly Methods for Forming 3D Mesostructures in Advanced Materials. *Nat. Rev. Mater.* **2017**, *2*, 17019−17035.

(39) Fu, H.; Nan, K.; Bai, W.; Huang, W.; Bai, K.; Lu, L.; Zhou, C.; Liu, Y.; Liu, F.; Wang, J.; Han, M.; Yan, Z.; Luan, H.; Zhang, Y.; Zhang, Y.; Zhao, J.; Cheng, X.; Li, M.; Lee, J. W.; Liu, Y.; et al.et al. Morphable 3D Mesostructures and Microelectronic Devices by Multistable Buckling Mechanics. *Nat. Mater.* **2018**, *17*, 268−279.

DOI: 10.1021/acsnano.8b06736
ACS Nano 2019, 13, 449−457

(40) Park, K.; Millet, L. J.; Kim, N.; Li, H.; Jin, X.; Popescu, G.; Aluru, N. R.; Hsia, K. J.; Bashir, R. Measurement of Adherent Cell Mass and Growth. *Proc. Natl. Acad. Sci. U. S. A.* **2010**, *107*, 20691−20696.
(41) Krishnan, S.; Shi, Y.; Webb, R. C.; Ma, Y.; Bastien, P.; Crawford, K. E.; Wang, A.; Feng, X.; Manco, M.; Kurniawan, J.; Tir, E.; Huang, Y.; Balooch, G.; Pielak, R. M.; Rogers, J. A. Multimodal Epidermal Devices for Hydration Monitoring. *Microsyst. Nanoeng.* **2017**, *3*, 17014−17025.
(42) Chung, S.; Park, S. Effects of Temperature on Mechanical Properties of SU-8 Photoresist Material. *Journal of Mechanical Science and Technology* **2013**, *27*, 2701−2707.
(43) Biswas, C. S.; Patel, V. K.; Vishwakarma, N. K.; Tiwari, V. K.; Maiti, B.; Maiti, P.; Kamigaito, M.; Okamoto, Y.; Ray, B. Effects of Tacticity and Molecular Weight of poly (N-isopropylacrylamide) on Its Glass Transition Temperature. *Macromolecules* **2011**, *44*, 5822−5824.
(44) Keddie, J. L.; Jones, R. A.; Cory, R. A. Size-Dependent Depression of the Glass Transition Temperature in Polymer Films. *Europhys. Lett.* **1994**, *27*, 59−64.
(45) Forrest, J. A.; Dalnoki-Veress, K.; Stevens, J. R.; Dutcher, J. R. Effect of Free Surfaces on the Glass Transition Temperature of Thin Polymer Films. *Phys. Rev. Lett.* **1996**, *77*, 2002−2005.
(46) Prucker, O.; Christian, S.; Bock, H.; Rühe, J.; Frank, C. W.; Knoll, W. On the Glass Transition in Ultrathin Polymer Films of Different Molecular Architecture. *Macromol. Chem. Phys.* **1998**, *199*, 1435−1444.
(47) Forrest, J. A.; Mattsson, J. Reductions of the Glass Transition Temperature in Thin Polymer Films: Probing the Length Scale of Cooperative Dynamics. *Phys. Rev. E: Stat. Phys., Plasmas, Fluids, Relat. Interdiscip. Top.* **2000**, *61*, 53−56.
(48) Forrest, J. A.; Dalnoki-Veress, K. The Glass Transition in Thin Polymer Films. *Adv. Colloid Interface Sci.* **2001**, *94*, 167−196.
(49) Dalnoki-Veress, K.; Forrest, J. A.; Murray, C.; Gigault, C.; Dutcher, J. R. Molecular Weight Dependence of Reductions in the Glass Transition Temperature of Thin, Freely Standing Polymer Films. *Phys. Rev. E: Stat. Phys., Plasmas, Fluids, Relat. Interdiscip. Top.* **2001**, *63*, No. 031801.
(50) Feng, R.; Farris, R. J. The Characterization of Thermal and Elastic Constants for an Epoxy Photoresist SU8 Coating. *J. Mater. Sci.* **2002**, *37*, 4793−4799.
(51) Kujawa, P.; Winnik, F. M. Volumetric Studies of Aqueous Polymer Solutions Using Pressure Perturbation Calorimetry: A New Look at the Temperature-Induced Phase Transition of poly (N-isopropylacrylamide) in Water and D_2O. *Macromolecules* **2001**, *34*, 4130−4135.
(52) Antipov, Y. V.; Vygodskii, Y. S. Polymers on the Basis of Epoxy Oligomers and Polyimides. *Moscow International Composites Conference (MICC) 90*; Springer: Dordrecht, 1991; pp 679−684.
(53) Ye, C.; Singh, G.; Wadley, M. L.; Karim, A.; Cavicchi, K. A.; Vogt, B. D. Anisotropic Mechanical Properties of Aligned polystyrene-block-polydimethylsiloxane Thin Films. *Macromolecules* **2013**, *46*, 8608−8615.

DOI: 10.1021/acsnano.8b06736
ACS Nano 2019, 13, 449−457